FULL PAPER

ADVANCED
FUNCTIONAL
MATERIALS

www.afm-journal.d

Check for
updates

Photoferroelectric Thin Films for Flexible Systems by a Three-in-One Solution-Based Approach

Iñigo Bretos,* Ricardo Jiménez, Jesús Ricote, Rafael Sirera, and M. Lourdes Calzada*

The effective incorporation of (multi)functional oxides into next-generation flexible electronics systems requires novel fabrication technologies that enable the direct integration of crystalline oxide layers in them. Unfortunately, this is considerably challenging due to the thermal incompatibility between the crystallization temperatures of metal oxides (>600 °C) and the thermal stability of the flexible polymer substrates conventionally used (<400 °C). Here, it is shown that $BiFeO_3$ thin films can be grown on flexible plastic by solution processing involving three different but complementary strategies to induce the crystallization of the perovskite phase at a lower temperature limit of 325 °C. This "three-in-one" approach is based on the synthesis of tailored metal precursors i) with a molecular structure resembling the crystalline structure of the oxide phase, which additionally allows both ii) photochemical and iii) internal combustion reactions taking place in the thin films. The flexible $BiFeO_3$ thin films obtained from a specifically designed molecular complex with *N*-methyldiethanolamine yield a large remnant polarization of 17.5 $\mu C\ cm^{-2}$, also showing photovoltaic and photocatalytic effects. This result paves the way for the direct integration of an interesting class of oxides with photoferroelectric properties in flexible devices with multiple applications in information and communication technology, and energy.

1. Introduction

Flexible electronics is one of the fastest growing technologies that our society is witnessing today.[1] The reason behind the emergence of this relevant platform lies in the different form that electronics is called to take in the near future: novel products are going to be created by placing electronic components on curved surfaces. This will allow a new generation of devices to be developed with disruptive applications in the fields of healthcare

and robotics (biomedical monitorization, prosthetic implants, electronic skin, etc.), energy (photovoltaic or harvesting systems for solar farms, vehicles, buildings, etc.), and information and communication technologies (wearable sensors, large-area displays, smart fabrics, etc.).[2] Whereas the "soft" nature of organic electronics turns them into main candidate materials for flexible devices at present, their performance and stability are major issues that still need to be addressed.[3] Therefore, other enabling materials and fabrication technologies are being required to satisfy the demands of next-generation flexible electronics systems.

In the last decade, thin films of inorganic materials have been demonstrated on flexible systems showing higher performance alternatives to their organic counterparts.[4] This is especially relevant for the large family of metal oxides, which display a wide range of properties (electrical, magnetic, and optical) and coupling effects (piezoelectricity, multiferroicity, magneto-electricity, and photoferroelectricity) with application in multiple devices as electronic components. With flexibility, a new dimension for the vast functionality of these materials is open provided their integration with a flexible system is accomplished. Although transfer printing techniques have been used in this context,[5] the complexity associated with some processing steps (particularly in subtractive mode) may increase the cost due to the need of sophisticated infrastructure. Also, the introduction of defects and contaminants during fabrication is another shortcoming of these techniques where device components are prefabricated on donor substrates (e.g., rigid silicon) and effectively transferred to the receiving substrate based on flexible polymers. The direct fabrication of functional metal oxides on flexible polymer substrates will overcome these problems. However, it entails nothing short of a technological challenge, i.e., the integration of inorganic materials conventionally processed at high temperatures with low melting point polymer substrates.

The functionality of most metal oxides relies on a crystalline structure that is usually obtained after high-temperature annealing (typically over 600 °C in the case of thin films). Flexible polymer substrates are not able to withstand such temperatures, and therefore novel pathways to induce the crystallization of the metal oxide layer at low temperature (<400 °C) have been explored over the last few years. Particularly, low-temperature approaches based on chemical solution deposition

Dr. I. Bretos, Dr. R. Jiménez, Dr. J. Ricote, Prof. M. L. Calzada
Instituto de Ciencia de Materiales de Madrid (ICMM-CSIC)
C/Sor Juana Inés de la Cruz 3, Madrid 28049, Spain
E-mail: ibretos@icmm.csic.es; lcalzada@icmm.csic.es
Dr. R. Sirera
Departamento de Química
Universidad de Navarra
C/Irunlarrea 1, Pamplona 31008, Spain

The ORCID identification number(s) for the author(s) of this article can be found under https://doi.org/10.1002/adfm.202001897.

(CSD) have shown promising results due to the great versatility they offer.[6] The different solution strategies reported in the literature aim at assisting the formation of a defect-free, highly densified metal–oxygen network in the as-deposited layer (by promoting the decomposition of organic compounds; the condensation among metal precursors; and the densification of the inorganic network), or the subsequent crystallization of the metal oxide thin film (by promoting the nucleation and growth of the crystal phase).[6b,7] The combination of some of these strategies is expected to reach impressive lower temperature limits for the crystallization of these materials. Thus, the low-temperature processing of functional oxide layers will not only allow the direct integration with flexible polymer substrates to be achieved, but it would also provide further environmental and economic benefits to the manufacturing system upon the reduction of the energy consumption of the fabrication process.[8]

Here, we report the direct growth of $BiFeO_3$ thin films on flexible polymer substrates showing multiple functionalities based on their ferroelectric, photovoltaic, and photocatalytic properties. This perovskite composition is among the few single-phase materials that display multiferroic properties (ferroelectricity and magnetism) at room temperature, which turns it into an excellent candidate for several applications in electronic components (transistors, diodes, integrated circuits, capacitors, inductors, sensors, and transducers).[9] In this work, a novel "three-in-one" approach to induce the crystallization of the oxide phase at low temperatures (325–350 °C) based on a solution processing method is presented. We specifically designed metal precursors that show three distinct chemical features suitable for the low-temperature processing of the corresponding thin films. The synthesis of molecular complexes formed by metal cations, bismuth (III) or iron (III), with alkanolamine ligands (*N*-methyldiethanolamine, MDEA) is the cornerstone of this approach.[10] First, the photosensitivity of the resulting precursors—hereinafter denoted as Bi-MDEA and Fe-MDEA—was exploited by a UV-assisted photoannealing process that promotes photochemical reactions in the thin films leading to the advanced decomposition of organic species from the chemical system, among other effects. The use of light as a complementary energy source to induce crystallization by photochemistry has been revealed in the last years as a powerful tool for the low-temperature processing of metal oxide layers.[11] Thus, high-energy photons coming from UV lamps can result in chemical bond cleavage (photolysis), formation of reactive species (oxygen radicals and ozone), and/or modification of the metal–oxygen network (condensation, densification, and crystallization).[6b,11a,12] Second, the choice of appropriate chemical reagents for the precursor solution of $BiFeO_3$ was observed to strongly influence the thermal decomposition of the corresponding thin films. A combustion reaction between the nitrate groups (i.e., the oxidizer) of the initial metal reagents and *N*-methyldiethanolamine (i.e., the fuel) would be responsible for the lower conversion temperatures required to obtain the oxide phase with respect to conventional systems (i.e., without compounds triggering an internal combustion reaction). This strong exothermic reaction is expected to provide a localized energy supply that would promote the complete decomposition of organic species from the system.[13] While this phenomenon has been demonstrated in solution-derived powders, a direct

evidence for such self-generated heat of synthesis in thin-film materials has not been shown yet.[14] The lower conversion temperatures actually achieved in metal oxide thin films are at the moment the best indication of the effectiveness of this combustion process instead.[15] Third, the resemblance between the molecular structure of the synthesized complexes and the crystalline structure of the corresponding metal oxides made this conversion to proceed with a relatively low energy input.[16] Chemical homogeneity of the solution joined to optimal interatomic bond distances and angles (with oxygen) in the metal precursors are known to facilitate the nucleation of the required crystal phase and to reduce the diffusion distance among nuclei. This allows the crystallization to be developed in a large sample volume in spite of the low-temperature regime applied, where the mobility of atoms is hindered. Finally, we demonstrated that the tailored precursors obtained from this "three-in-one" solution-based approach—where the combination of different but complementary low-temperature strategies is achieved—resulted in the fabrication of flexible $BiFeO_3$ thin films with photoferroelectric properties of potential application in memory, photovoltaic, or photocatalytic devices.

2. Results and Discussion

2.1. Bi-MDEA and Fe-MDEA Precursors

As it has been explained in the Introduction, in this novel approach the chosen precursors must comply with the requirements of three different but complementary strategies to induce the low-temperature crystallization of the respective oxides. Starting with metal nitrates as initial reagents, the choice of an adequate complexing agent is thus crucial. In a previous study, the photosensitivity of several alkanolamine and aldehyde complexing agents was analyzed with regard the low-temperature processing of $PbTiO_3$ thin films, concluding the superior properties of the former.[17] MDEA offers in principle at least two of the characteristics required for this "three-in-one" approach: it yields photosensitive precursors and it promotes combustion reactions with the nitrate groups already present in the system. These two features have been analyzed for the Bi-MDEA and Fe-MDEA precursors of this work, together with the resemblance between their molecular structure and the crystalline structure of their corresponding oxides, the third low-temperature strategy of this approach.

The details of the synthesis of the Bi-MDEA and Fe-MDEA precursors are described in the Experimental Section of this manuscript. Both initial reagents, nitrate salts of bismuth (III) and iron (III), were reacted with the complexing agent MDEA. The crucial formation of a photosensitive complex between the metal cation and the alkanolamine ligand where electronic transitions are induced by visible light absorption could be inferred from empirical evidence, since both solutions developed a characteristic brown ocher color (Figure S2, Supporting Information). The observation of color changes during the synthesis was much clearer for the bismuth system, which evolved from a colorless solution to the final brownish color (Movie S3, Supporting Information). While the appearance of color is commonly associated with the presence of d–d transitions (typically
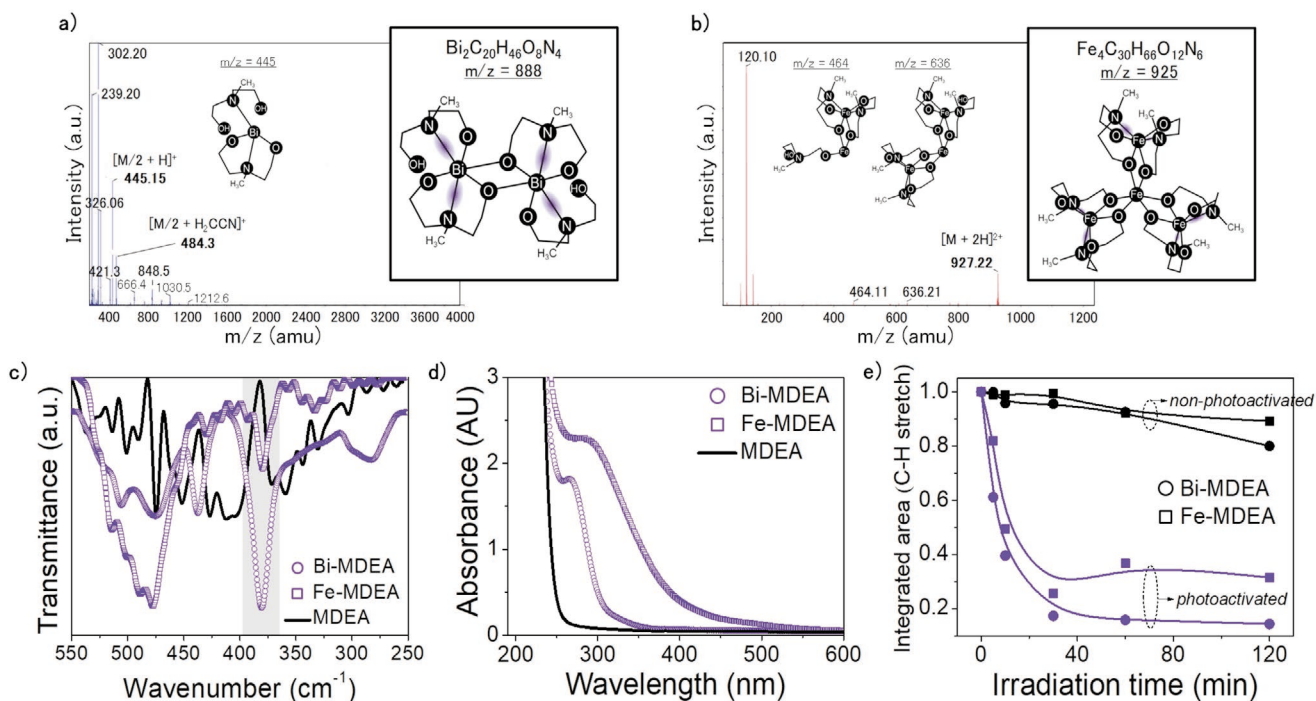
Figure 1. Molecular structure and photochemical properties of the Bi-MDEA and Fe-MDEA precursors. ESI-MS spectra and molecular structures proposed for the a) Bi-MDEA and b) Fe-MDEA metal complexes. c) FTIR spectra of the metal precursors, where the stretching ν(M—N) mode appears highlighted (M = Bi or Fe). d) UV/vis absorption spectra of the metal precursors showing the charge-transfer bands associated with the M—N chemical bond (M = Bi or Fe). e) Evolution of the relative integrated area corresponding to the C—H stretching vibration bands of photoactivated and non-photoactivated Bi-MDEA and Fe-MDEA thin films as a function of irradiation time.

observed in transition metals with partially filled d orbitals), this is especially relevant for the Bi-MDEA complex formed by Bi(III) with completely filled d orbitals. In this case, electronic charge would be transferred between the metallic center and the MDEA ligand by a different transition giving rise to charge transfer bands that cause color. A similar situation occurs for the Fe-MDEA complex (charge transfer would occur now from the MDEA ligand to the partially filled d orbital of the metallic center), where a fast exothermic reaction between the metal nitrate and the MDEA compound upon mixing was additionally noticed. To determine the molecular structure of the metal complexes, electrospray ionization mass spectroscopy (ESI-MS) was used for the analysis of the respective precursor solutions. The main advantage of this technique is that it is based on a soft ionization process whereby macromolecules are not fragmented into smaller species, so they can be directly detected by mass spectroscopy afterward. The resulting spectra are shown in **Figure 1**, where the molecular structures proposed for each metal complex are depicted. These are supported by the presence of signals corresponding to specific fragments derived from it (m/z = 445 for Bi-MDEA; Figure 1a) or to the metal complex itself (m/z = 927 for Fe-MDEA; Figure 1b). A ratio between the metallic center and the MDEA ligand of 1:2 and 1:1.5 is thus obtained for the respective Bi-MDEA and Fe-MDEA complexes. The molecular structure proposed for these metal complexes in solution agrees well with that previously determined by X-ray diffraction (XRD) on the corresponding single crystal derivatives.[18] Analysis of chemical shifts from nuclear magnetic resonance (1H-NMR and 13C-NMR) spectra

complementary supports their structure (Figure S4, Supporting Information).[10a]

One of the most significant features of the precursors synthesized in this work, particularly for the Bi-MDEA one, is the appearance of color in the solution. From the previous analyses, the molecular structure of these metal complexes shows metal–nitrogen bonds that would be responsible for light absorption. Figure 1c shows the respective Fourier transformed infrared (FTIR) spectra, where vibration bands ascribed to this chemical bond are observed. The stretching ν(M—N) mode, where M stands for either Bi or Fe, is specifically detected at wavelengths of 385–370 cm^{-1}. The absorption spectra measured by ultraviolet–visible (UV/vis) spectroscopy for the Bi-MDEA and Fe-MDEA precursors are shown in Figure 1d. In both cases, an absorption band in the UV region ($\approx$270 nm) is observed that can be associated with electronic transitions between the metallic center and the MDEA ligand. Note that this band is not present in the UV/vis spectrum of the MDEA compound, supporting the formation of the light-sensitive metal complexes of this work.

The presence of these metallic complexes in the solutions provides a chemical system that is capable of undergoing intended effects by photochemistry upon UV illumination.[10] To study the photochemical effects in the thin films, layers from the former Bi-MDEA and Fe-MDEA precursors were deposited on silicon substrates and subjected to UV irradiation at 150 °C (see the Experimental Section). Figure 1e depicts the evolution with irradiation time of the relative integrated areas corresponding to the C—H stretching vibration bands measured in the respective films by FTIR spectroscopy (Figure S5, Supporting Information).

**ADVANCED
SCIENCE NEWS**

www.advancedsciencenews.com

**ADVANCED
FUNCTIONAL
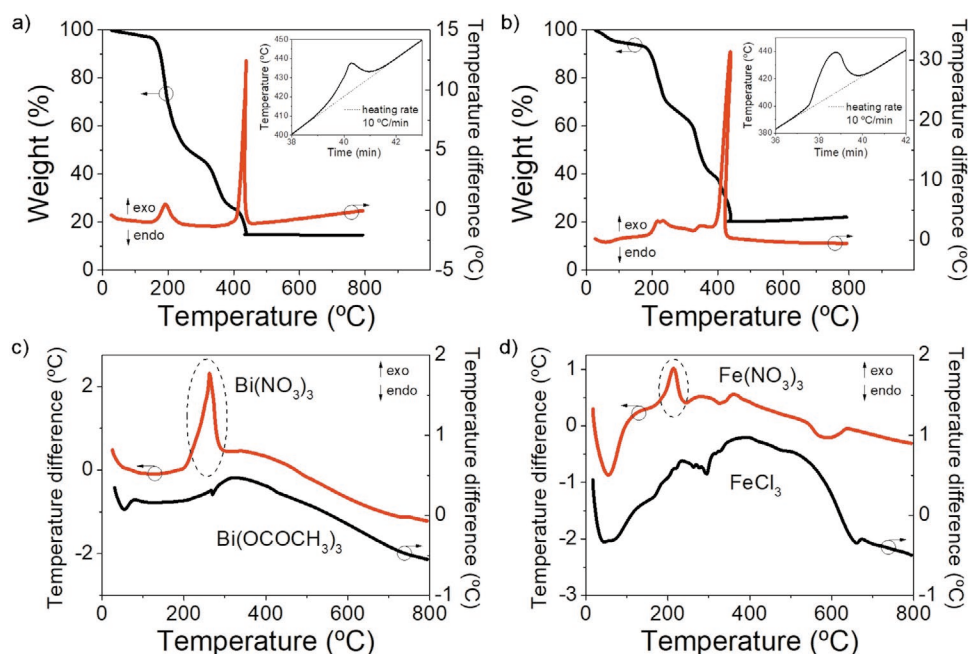MATERIALS**

www.afm-journal.de

Figure 2. Thermal decomposition and combustion characteristics of the Bi-MDEA and Fe-MDEA precursors. TGA/DTA curves measured in air of the a) Bi-MDEA and b) Fe-MDEA precursors (insets show the deviation from the heating rate recorded by the equipment). DTA curves measured in argon of the c) Bi-MDEA and d) Fe-MDEA precursors synthesized from different metal reagents (nitrates and either acetate or chloride salts; see the Experimental Section), where the exothermic signal appears highlighted.

A clear decrease in such areas for both Bi-MDEA and Fe-MDEA films is observed denoting the photochemical cleavage of the C−H bonds. This effect is indicative of the decomposition of the organic compounds (alkanes) present in the system promoted by several processes induced by UV light.[19] After 30 min of irradiation, similar values are reached in each graph denoting a steady state achieved in the samples under these irradiation conditions. Note that the same experiment without UV irradiation results in a practically constant content of organic species in the system over time. The advanced decomposition of the metal precursors achieved by this strategy (using light instead of heat) would therefore contribute to the early-stage formation of an amorphous metal–oxygen network in the system. Crystallization of the oxide phase from the former state is known to proceed with a relatively low thermal input that would result in a lower processing temperature finally required.[6b,11a]

The thermal decomposition of the Bi-MDEA and Fe-MDEA precursors was investigated by the thermogravimetric analysis (TGA) and differential thermal analysis (DTA) shown in **Figure 2**. Figure 2a,b depicts the respective curves measured in air of the gel powders derived from the corresponding solutions. Whereas most of the organic compounds are decomposed between 200 and 400 °C, a strong exothermic peak around 438 °C is observed in both systems with an abrupt mass loss associated. This process provides an internal supply of energy to the system that even raises the temperature recorded by the equipment (see insets). Considering the chemical species present in the system, a combustion reaction can likely occur between the MDEA and the nitrate groups of the initial metal reagents, which would behave as the respective fuel and oxidant agents needed for this redox-based highly exothermic

chemical reaction. Complementary thermal analysis experiments carried out in argon are shown in Figure 2c (DTA curves for Bi-MDEA) and Figure 2d (DTA curves for Fe-MDEA), where the presence of a single exotherm (≈215 °C) supports the aforementioned combustion process. On the contrary, no exothermic peak is observed when a different salt is used for the metal precursor instead of nitrate (bismuth acetate and iron chloride, curves in black in Figure 2c,d) or when MDEA is not present in the system (not shown). This fact corroborates that both oxidizer and fuel are already contained in the Bi-MDEA and Fe-MDEA precursors of this work. The self-generated heat developed in the nitrate-containing system by combustion reaction is responsible for the lower temperatures required for the complete conversion to the metal oxide: from a temperature readout around 438 °C versus ≈478 °C by using bismuth (III) acetate or even ≈570 °C by using iron (III) chloride (Figure S6, Supporting Information). Thus, combustion chemistry would supply enough energy to decompose all the organic species present in the system before forming the corresponding metal oxide. Under this scenario the crystallization of the final oxide phase may be induced at lower temperatures, which is the basis of this chemical strategy.[15]

During the decomposition step assisted by both photochemical and combustion reactions, the organic moieties of the Bi-MDEA and Fe-MDEA precursors are eliminated leaving the metal cations and oxygen as the only species remaining in the system.[20] The subsequent crystallization into the corresponding oxide phase (i.e., Bi_2O_3 and Fe_2O_3) is governed by the diffusion of the respective atoms in a process that is strongly temperature-dependent. As stated in the Introduction, the formation of an optimum metal–oxygen network with an
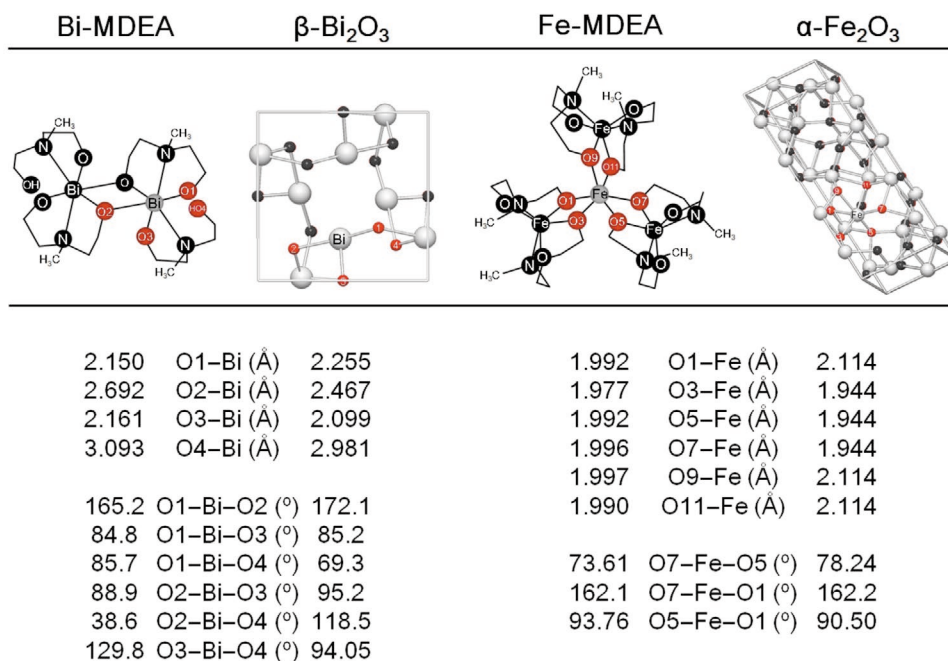
Bi-MDEA	β-Bi_2O_3	Fe-MDEA	α-Fe_2O_3

2.150	O1–Bi (Å)	2.255		1.992	O1–Fe (Å)	2.114
2.692	O2–Bi (Å)	2.467		1.977	O3–Fe (Å)	1.944
2.161	O3–Bi (Å)	2.099		1.992	O5–Fe (Å)	1.944
3.093	O4–Bi (Å)	2.981		1.996	O7–Fe (Å)	1.944
				1.997	O9–Fe (Å)	2.114
165.2	O1–Bi–O2 (°)	172.1		1.990	O11–Fe (Å)	2.114
84.8	O1–Bi–O3 (°)	85.2				
85.7	O1–Bi–O4 (°)	69.3		73.61	O7–Fe–O5 (°)	78.24
88.9	O2–Bi–O3 (°)	95.2		162.1	O7–Fe–O1 (°)	162.2
38.6	O2–Bi–O4 (°)	118.5		93.76	O5–Fe–O1 (°)	90.50
129.8	O3–Bi–O4 (°)	94.05				

Figure 3. Resemblance between the molecular structure of the Bi-MDEA and Fe-MDEA precursors and the crystalline structure of their corresponding metal oxides. Selected bond lengths and angles of the corresponding chemical structures have been taken from the literature[17] and a crystallographic database.[21]

arrangement of atoms nearly identical to the structure of the crystal phase would facilitate the nucleation in the thin film by reducing the atomic diffusion length required to form the crystalline oxide in a low-temperature regime. **Figure 3** shows the structure of the molecular complexes of this work and that of their corresponding crystalline oxides, where selected bond lengths and angles appear highlighted in red for the sake of comparison. Structural data of the Bi-MDEA and Fe-MDEA precursors have been collected from the literature,[18] whereas a crystallographic database[21] has been used for the respective metal oxides. For the last ones, tetragonal β-Bi_2O_3 (fluorite-based) and rhombohedral α-Fe_2O_3 (hematite) structures were chosen according to the X-ray diffraction of the crystalline films obtained after annealing of Bi-MDEA and Fe-MDEA precursor layers at 600 °C (Figure S7, Supporting Information). Attending to the data shown in the figure, a clear correlation can be inferred from the molecular structure of the metal complexes and the crystalline structure of their corresponding metal oxides. Although small deviations are observed in some bond distances and angles, the resemblance between the respective molecular and crystalline structures is relatively high for both systems: the comparison with other polymorphs of Bi_2O_3 and Fe_2O_3 resulted in a stronger discrepancy between data (not shown). The optimum arrangement of atoms in these Bi-MDEA and Fe-MDEA precursors, with a homogeneous distribution of molecular clusters containing Bi (III), Fe (III), and oxygen, is expected to facilitate the mass transport required to form the crystalline oxide by atomic diffusion under a kinetic regime that would be limited by the use of low processing temperatures. From all these results we can conclude that the rational design of the Bi-MDEA and Fe-MDEA precursors of this work, combining the three aforementioned strategies, fulfills the

requirements to proceed with the fabrication of $BiFeO_3$ thin films at a low temperature limit.

2.2. $BiFeO_3$ Thin Films

A precursor solution of $BiFeO_3$ was obtained from the aforementioned Bi-MDEA and Fe-MDEA low-temperature precursors. The growth of crystalline $BiFeO_3$ thin films from this solution onto flexible polymer substrates (polyimide) was carried out by photochemical solution deposition (PCSD) using light as a complementary energy source to induce crystallization instead of a conventional high-temperature treatment. **Figure 4**a shows the X-ray patterns of $BiFeO_3$ thin films processed at different temperatures (≤350 °C) on silicon substrates with and without an intermediate UV irradiation step (see the Experimental Section). Reflections corresponding to the perovskite phase appear in the photoactivated films, whereas the nonirradiated counterparts remain amorphous to XRD. Tuning certain processing conditions (e.g., multiple deposition leading to different film thicknesses) can even decrease the crystallization temperature of the $BiFeO_3$ thin films down to such a low value of 325 °C. The advanced decomposition of these precursors promoted by both photochemical and combustion reactions would be responsible for the formation of the amorphous metal–oxygen network in the system at an earlier stage. The local arrangement of these atoms, close to the perovskite structure of the corresponding metal oxide, would account for the lower energy via thermal treatment required for the complete crystallization of single-phase films (185 nm thick) afterward (Figure 4b).Thus, the low-temperature processing employed here allowed the direct growth of $BiFeO_3$ perovskite films on
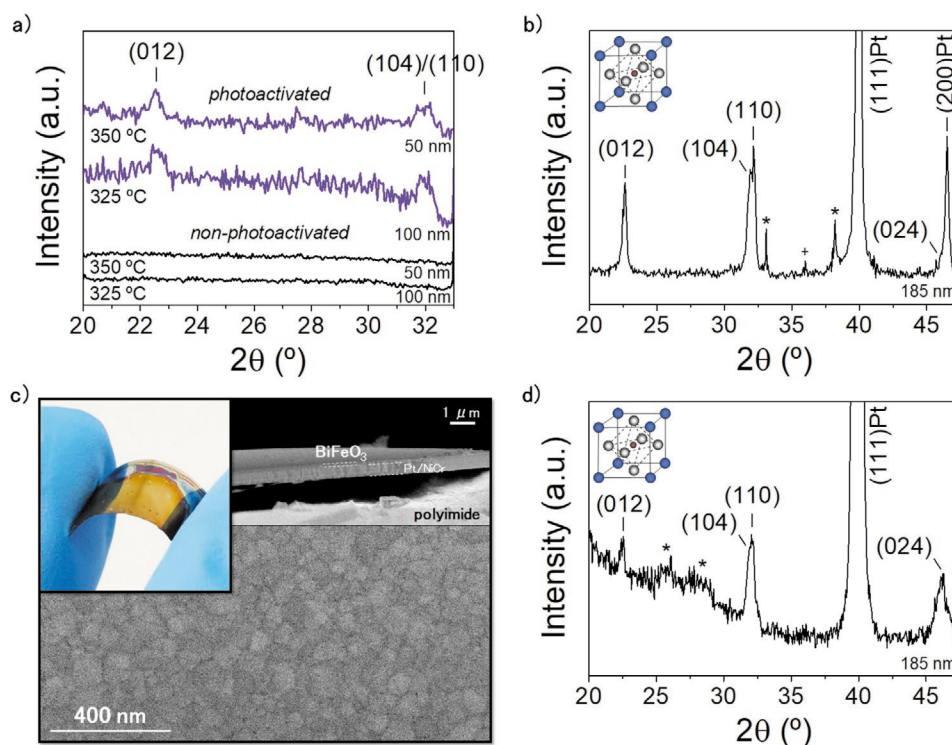
Figure 4. Crystalline structure and microstructure of the low-temperature processed $BiFeO_3$ thin films. a) XRD patterns of photoactivated and non-photoactivated thin films annealed at different temperatures on $Pt/TiO_2/SiO_2/(100)Si$ substrates. b) XRD pattern of the $BiFeO_3$ thin film annealed at 325 °C on a $Pt/TiO_2/SiO_2/(100)Si$ substrate, where reflections corresponding to the perovskite phase are indexed (* = substrate, + = K_β (111)Pt). c) SEM images of the $BiFeO_3$ thin films annealed at 325 °C, together with a photograph of the flexible sample (2×1 cm^2). d) XRD pattern of the flexible $BiFeO_3$ thin film annealed at 325 °C on a Pt/Cr/PI/NiCr/Pt substrate, where reflections corresponding to the perovskite phase are indexed (* = substrate).

flexible polymer substrates to be achieved. Note that temperature values reported from the literature for most $BiFeO_3$ thin films prepared by conventional processing are over 500 °C,[22] which result not compatible with thermosensitive substrates such as those based on flexible polymers. Figure 4c shows the microstructural observation by scanning electron microscopy (SEM) of the $BiFeO_3$ thin films crystallized at 325 °C on flexible polyimide. A polycrystalline microstructure consisting of rounded grains with an average size of ≈55 nm forms the surface morphology of these films. Regions with different contrasts associated with differentiated phases (secondary phases, rests of organic compounds) are not observed in the micrograph of the film surface. The film thickness calculated from the cross-section micrograph is ≈185 nm, which agrees with the values measured by profilometry (not shown). Note that the flexible nature of the polymer substrate (see photograph of Figure 4c) imposes restrictions on the cross-sectional cut of the sample, which cannot be done efficiently without the collapse of the different constituent layers, thus hampering a more detailed analysis on the heterostructure of this film. The X-ray pattern of this flexible thin film is shown in Figure 4d. The film denotes no secondary phases, showing a pseudocubic (theoretically indexed as rhombohedral) perovskite structure in agreement with the previous results for the analogous film prepared on a silicon substrate (see Figure 4b).

The ferroelectric properties of the flexible $BiFeO_3$ thin film processed at 325 °C are evaluated from the hysteresis loops shown in **Figure 5**. The presence of defect complexes

(oxygen-vacancy-associated dipoles) in the film may be responsible for the leakage current contribution observed in the experimental loop, as we previously reported.[23] Nonswitching contributions arisen from linear capacitance and resistance effects, as well as from nonlinear conduction (leakage current), are subtracted from the experimental loop by a simulation model using a fitting algorithm based on an implemented hyperbolic tangent function.[24] A remanent polarization of 17.5 μC cm^{-2} is obtained at room temperature with a coercive field of 525 kV cm^{-1} (Figure 5a), supporting the potential application of these films for data storage in nonvolatile memories integrated in next-generation flexible devices.[2e] Similar polarization values (P_r = 21.5 μC cm^{-2}) were measured in a low-temperature processed film prepared from the same precursor solution on a rigid Si substrate (Figure S8, Supporting Information), which suggests that the method reported here could be transferred to substrates of different nature (e.g., glass and metal foils). On the other hand, a larger remanent polarization (P_r = 27.5 μC cm^{-2}) is obtained in the flexible $BiFeO_3$ thin film measured at 128 K (Figure 5b). This is due to the reduction of the high electrical conductivity and leakage current typically associated with this material during the poling process at room temperature, which lead to detrimental switching of ferroelectric domains. Regardless of this effect, the shape of the current density plot of Figure 5a clearly evidences the intrinsic polarization characteristics of the flexible $BiFeO_3$ thin film prepared at only 325 °C. This demonstrates the validity of this processing method to induce the crystallization at temperatures well below
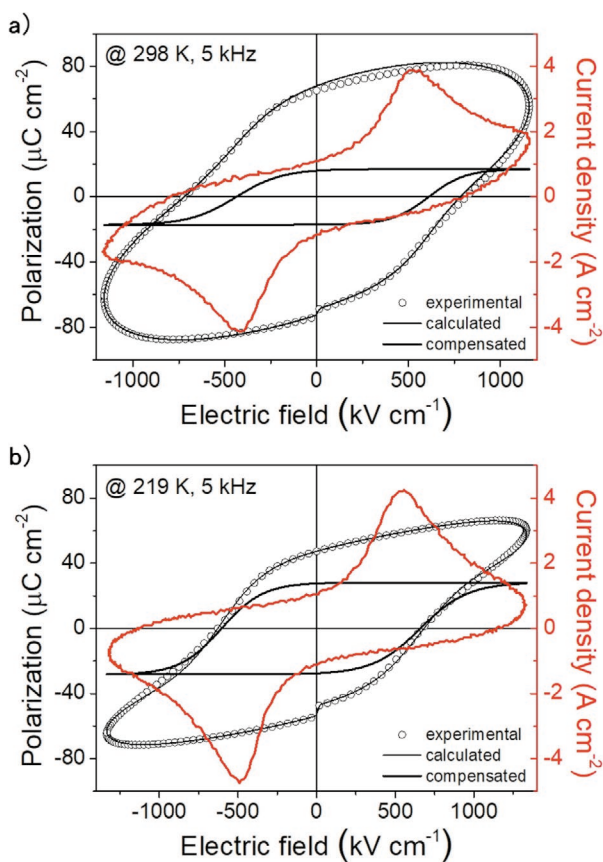
**ADVANCED
SCIENCE NEWS**
www.advancedsciencenews.com

**ADVANCED
FUNCTIONAL
MATERIALS**
www.afm-journal.de

Figure 5. Ferroelectric hysteresis loops of the flexible BiFeO₃ thin film annealed at 325 °C. a) Hysteresis loops of polarization and current density versus electric field measured at room temperature (298 K) and 5 kHz. b) Hysteresis loops of polarization and current density versus electric field measured at low temperature (219 K) and 5 kHz. The compensated polarization loops are included in each graph, where the non-switching contributions derived from leakage current and conductivity have been subtracted after calculation.

the conventional values used in the fabrication of these functional materials on rigid substrates.

The relatively low bandgap of the BiFeO₃ perovskite (2.2–2.7 eV) turns it into a promising ferroelectric material with potential photoconductivity and a conventional photovoltaic effect.[25] **Figure 6** depicts the *J–V* curves of a flexible BiFeO₃ thin film measured at different experimental conditions of temperature, illumination and poling state. Both the current and the voltage measured in the capacitor are significantly affected by the illumination of the sample with time (Figure S9, Supporting Information). A clear photovoltaic effect is observed from Figure 6a, where illumination under a high-intensity light source (420 nm laser) yields a short-circuit current density of 0.015 mA cm⁻² and an open-circuit voltage of 0.036 V at room temperature. Despite these values being lower than those usually obtained in conventional BiFeO₃ thin films prepared at high temperatures, this is the first time that a photovoltaic behavior is demonstrated in a flexible ferroelectric thin film prepared at such a low temperature. Both photoinduced current and voltage were found to increase in magnitude as poling of the sample was effectively carried out at low temperature (Figure 6b). The

short-circuit current density and open-circuit voltage reach now respective values of 0.036 mA cm⁻² and 0.44 V after poling with 34 V at 128 K. In a previous work, we showed that poling at low temperature is necessary for the effective depinning and subsequent switching of ferroelectric domains in solution-processed BiFeO₃ thin films.[23] The release of mobile, free species after depinning would be responsible for the larger photocurrent generated in the material. The improvement on domain mobility also results in a larger contribution to ferroelectric switching that can be inferred from the higher value of remanent polarization obtained when compared to that measured at room temperature (see Figure 5). As a consequence, the photovoltage generated in the flexible film after poling at low temperature is significantly enhanced with respect to room temperature (0.44 V vs 0.036 V). The demonstration of a photovoltaic effect in the ferroelectric films of this work could open new possibilities in the energy storage options for self-powering devices based on flexible memories, sensors, and/or actuators, where high energy conversions are in principle not needed.[26]

Apart from photovoltaics, other photoinduced effects in ferroelectrics may provide additional functionalities and/or coupling phenomena to these materials with high potential for novel and future applications in different fields. This is the case of the photocatalytic activity shown by the flexible BiFeO₃ films of this work. Ferroelectric oxides can be considered as wide bandgap semiconductors with internal electric fields that can mitigate the adverse recombination of photogenerated carriers, thus improving the photocatalytic efficiency.[27] Particularly, the BiFeO₃ perovskite exhibits a relatively low bandgap that also turns it into an excellent photocatalyst under visible light irradiation.[28] Figure 6c shows the degradation of the organic dye methylene blue (MB) over a flexible BiFeO₃ thin film by photocatalytic oxidation using visible light. After 600 min of irradiation, the degradation rate of MB (calculated from the relative integrated area of the absorption bands between 550 and 700 nm) reached 76% (Figure 6d), which was more than twice the value obtained without the sample (i.e., blank). Note that MB remains practically unaltered when using commercial particles of the traditional photocatalyst TiO₂, since the bandgap of this metal oxide is too high (>3.0 eV) to absorb visible light. Illumination with UV light would therefore be required, loosing thus the 45% of the solar spectrum that could be used to degrade organic pollutants or generate hydrogen in a sustainable energy cycle. The photocatalytic activity of these BiFeO₃ thin films may provide significant benefits to the industrial sector in terms of economic cost upon the use of cheap, lightweight, and flexible polymer substrates.[29] Additionally, novel applications based on flexible photocatalytic systems could be opened in construction and energy (e.g., self-cleaning windows and efficient solar panels) and environmental remediation (e.g., external transparent pipes for wastewater treatment), where the economical and toxicity problems typically associated with the removal of photocatalytic nanoparticles from the system would be avoided.

3. Conclusion

The direct integration of BiFeO₃ thin films as active layers into flexible electronic systems can be accomplished by a solution
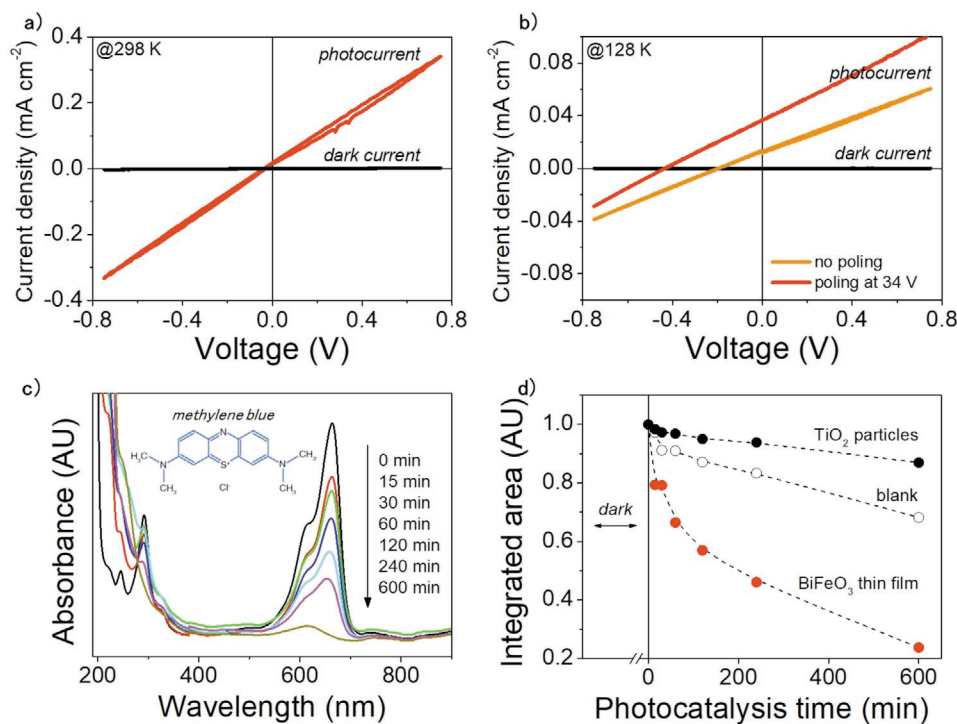
Figure 6. Photovoltaic and photocatalytic properties of the flexible $BiFeO_3$ thin films. Current–voltage characteristics with and without illumination measured a) at room temperature and b) at low temperature (128 K) under different poling conditions. c) Evolution with time of the UV/vis absorption spectra of methylene blue on a flexible $BiFeO_3$ thin film under visible illumination. d) Evolution of the relative integrated area corresponding to the 550–700 cm^{-1} absorption bands of methylene blue under visible light by a flexible $BiFeO_3$ thin film as a function of photocatalysis time.

processing method based on a facile, low-cost fabrication approach. Tailored precursors are synthesized to combine simultaneously three complementary strategies to lower the crystallization temperature of the system. The chemical features required are 1) a suitable molecular structure, 2) photosensitivity, and 3) internal combustion reactants (oxidizer and fuel). These are demonstrated in the molecular complexes formed between the metallic centers, Bi (III) or Fe (III), and MDEA that serve as metal precursors in this work. The decomposition of such precursors is enhanced by both photochemical and combustion reactions in an intermediate UV-assisted photoannealing step, whereas the structural similarities between the molecular complex and the corresponding metal oxide reduce the atomic diffusion needed to form the crystal, thus facilitating the crystallization of the $BiFeO_3$ perovskite at only 325 °C. The $BiFeO_3$ thin films directly grown on flexible polymer substrates with this novel method show ferroelectric, photovoltaic, and photocatalytic behavior, which makes them suitable for the effective integration of photoferroelectrics in new flexible electronics devices. To the best of our knowledge, this is the first time that a flexible photoferroelectric is demonstrated.

4. Experimental Section

Synthesis of Precursor Solutions: The flow charts of the two synthesis routes leading to the Bi-MDEA and Fe-MDEA precursors are shown elsewhere (Figure S1, Supporting Information). Bismuth (III) nitrate pentahydrate ($Bi(NO_3)_3 \cdot 5H_2O$, ≥99.99% trace metals basis, Sigma-Aldrich), iron (III) nitrate nonahydrate ($Fe(NO_3)_3 \cdot 9H_2O$, ≥99.95%

trace metals basis, Sigma-Aldrich), *N*-methyldiethanolamine ($CH_3N(CH_2CH_2OH)_2$, ≥99%, Sigma-Aldrich), 1,3-propanediol ($HO(CH_2)_3OH$, 98%, Sigma-Aldrich), and dried ethanol (CH_3CH_2OH, SeccoSolv, max. 0.01% H_2O, Merck Chemicals) were used as starting reagents. Metal nitrates were first dissolved at room temperature in a mixture of MDEA and 1,3-propanediol solvents using a molar ratio of 1:5:10 (metal:MDEA:diol). The addition of 1,3-propanediol was observed to stabilize the resulting solutions by preventing uncontrolled condensation reactions among molecular species that led to undesired precipitation/gelification of the system, most likely due to the coordinating properties of this diol. Complexing reactions between the MDEA and the respective metal ions was promoted by heating the mixture at 150 °C for 120 min and further heating under reflux at 190 °C for 10 min. After diluting with ethanol, stable solutions of Bi-MDEA and Fe-MDEA precursors were obtained with a concentration of 0.3 м. Stoichiometric amounts of these solutions were mixed together to prepare a precursor solution of $BiFeO_3$ (0.3 м). Bi-MDEA and Fe-MDEA precursors using bismuth (III) acetate ($Bi(CH_3COO)_3$, ≥99.99% trace metals basis, Sigma-Aldrich) and iron (III) chloride ($FeCl_3$, 97%, Sigma-Aldrich) as the respective starting reagents instead of the metal nitrates were also synthesized using the same procedure described before.

Characterization of Bi-MDEA and Fe-MDEA Precursors: ESI-MS was performed using a quadrupole time-of-flight hybrid mass spectrometer (QStar instrument, AB Sciex) operating in positive mode with an ESI source voltage of 5.5 kV. Aliquots from the respective solutions of the Bi-MDEA and Fe-MDEA precursors were diluted (20 ppm) with acetonitrile for the measurements. Nuclear magnetic resonance (NMR) spectroscopy of ^1H and ^{13}C nuclei was also carried out (DRX 500 instrument, Bruker) in the solutions using deuterated methanol/chloroform as solvents. UV/vis absorption spectroscopy was conducted (Libra S35 instrument, Biochrom) in aliquots from the liquid precursors diluted with dried ethanol(10^{-4} м). FTIR spectroscopy was performed (IFS66v/S instrument with DTGS detector, BrukerOptics) on gel powders

**ADVANCED
SCIENCE NEWS**

www.advancedsciencenews.com

**ADVANCED
FUNCTIONAL
MATERIALS**

www.afm-journal.de

derived from the respective solutions of the Bi-MDEA and Fe-MDEA precursors dried at 150 °C overnight, which were also subjected to TGA and DTA under different atmospheres (Q600 instrument, TA Instruments). XRD was also carried out (D8 ADVANCE instrument, Cu Kα radiation, Bruker) on powders annealed at different temperatures to detect the presence of crystalline phases.

Fabrication of Thin Films: For the photochemical study of this work, a single layer from a 0.1 M solution of the respective Bi-MDEA and Fe-MDEA liquid precursors was deposited on double side polished Si (100) substrates by spin coating (2000 rpm for 45 s). The resulting wet films were dried on a hot plate at 150 °C for 5 min and subjected to UV irradiation for different times in oxygen at 150 °C in a laboratory-scale equipment with a high-intensity excimer lamp (222 nm, BlueLight Heraeus Excimer System). In the case of the BiFeO$_3$ system, layers from the respective precursor solution were deposited on Pt/TiO$_2$/SiO$_2$/(100)Si substrates by spin coating (2000 rpm for 45 s). The resulting wet films were dried on a hot plate at 150 °C for 5 min and subjected to UV irradiation in oxygen at 150 °C for 30 min. The amorphous films obtained were crystallized at different temperatures for 60 min in oxygen by rapid thermal annealing (30 °C s^{-1}, JIPELEC JetStar 100T Processor). For the fabrication of the flexible BiFeO$_3$ thin film, layers from the respective precursor solution were deposited on polymer Pt/Cr/PI/NiCr/Pt substrates (75 m thick UPILEX-S polyimide, UBE Industries Ltd.) by dip coating (150 mm min^{-1} withdrawal speed). Drying, irradiation, and crystallization of the film were identically carried out as the analogous films deposited on silicon substrates. To grow films with a certain thickness, multiple depositions whereby each single layer was successively deposited, dried, irradiated, and crystallized was carried out.

Characterization of Thin Films: FTIR spectroscopy was performed (IFS66v/S instrument, Bruker Optics) in the thin films deposited on double side polished Si (100) substrates. XRD was carried out (D8 ADVANCE instrument, Cu Kα radiation, Bruker) in thin films annealed at different temperatures to detect the presence of crystalline phases. The surface morphology and microstructure of the films was observed by scanning electron microscopy (Nova NanoSEM 230 instrument, FEI Company). For the electrical characterization, a planar array of discrete capacitors was fabricated by sputter deposition of top Pt electrodes onto the film surfaces through a shadow mask. Ferroelectric hysteresis loops were measured with a virtual ground system composed by a pulse generator (33220A Arbitrary Waveform Generator, Agilent), a power amplifier (High-Voltage Amplifier 9100, Tabor Electronics), a current amplifier (428-PROG Programmable Current Amplifier, Keithley), and an oscilloscope (TDS 520, Tektronix). The charge loops were obtained by numerical integration from the respective current loops. Photovoltaic properties were analyzed from the variation of the current density with voltage under different conditions of temperature, illumination, and poling state using an electrochemical interface (PalmSens4, PalmSens) with a laser light source (420 nm, 15 mW) focused on a spot area of ≈1 mm^2. The photocatalytic activity was evaluated by analyzing the degradation of methylene blue (C$_{16}$H$_{18}$ClN$_3$S·xH$_2$O, Sigma-Aldrich) using a solar lamp (Ultra-Vitalux 300 W, Osram) emitting in UVA (13.6 W) and UVB (3.0 W) regions. To perform the analysis under visible light, plastic (acrylic) sheeting was used to filter the UV radiation. The thin-film sample (2 cm^2 area, 185 nm thickness) was placed inside a reactor chamber filled with 8 mL of the dye solution (10^{-4} M) with pH ≈1 (fixed with HCl) to avoid photobleaching effect. The solution was irradiated for different times and further analyzed by UV/vis absorption spectroscopy (Libra S35 instrument, Biochrom). The temperature in the reactor was kept below 38 °C by a cooling system during the whole experiment.

Supporting Information

Supporting Information is available from the Wiley Online Library or from the author.

Conflict of Interest

The authors declare no conflict of interest.

[1] a) Y. S. Rim, S.-H. Bae, H. Chen, N. De Marco, Y. Yang, *Adv. Mater.* **2016**, *28*, 4415; b) A. Nathan, A. Ahnood, M. T. Cole, S. Lee, Y. Suzuki, P. Hiralal, F. Bonaccorso, T. Hasan, L. Garcia-Gancedo, A. Dyadyusha, S. Haque, P. Andrew, S. Hofmann, J. Moultrie, D. Chu, A. J. Flewitt, A. C. Ferrari, M. J. Kelly, J. Robertson, G. A. J. Amaratunga, W. I. Milne, *Proc. IEEE* **2012**, *100*, 1486; c) W. S. Wong, A. Salleo, *Flexible Electronics: Materials and Applications*, Springer, New York **2009**; d) S. Yugang, J. A. Rogers, *Adv. Mater.* **2007**, *19*, 1897.

[2] a) M. Bariya, H. Y. Y. Nyein, A. Javey, *Nat. Electron.* **2018**, *1*, 160; b) A. Chortos, J. Liu, Z. Bao, *Nat. Mater.* **2016**, *15*, 937; c) F. R. Fan, W. Tang, Z. L. Wang, *Adv. Mater.* **2016**, *28*, 4283; d) S. Bauer, S. Bauer-Gogonea, I. Graz, M. Kaltenbrunner, C. Keplinger, R. Schwödiauer, *Adv. Mater.* **2014**, *26*, 149; e) S.-T. Han, Y. Zhou, V. A. L. Roy, *Adv. Mater.* **2013**, *25*, 5425; f) J. Lee, J. Wu, M. Shi, J. Yoon, S.-I. Park, M. Li, Z. Liu, Y. Huang, J. A. Rogers, *Adv. Mater.* **2011**, *23*, 986.

[3] a) M. L. Hammock, A. Chortos, B. C.-K. Tee, J. B.-H. Tok, Z. Bao, *Adv. Mater.* **2013**, *25*, 5997; b) S. Wagner, S. Bauer, *MRS Bull.* **2012**, *37*, 207.

[4] a) W. Liu, M. Liu, R. Ma, R. Zhang, W. Zhang, D. Yu, Q. Wang, J. Wang, H. Wang, *Adv. Funct. Mater.* **2018**, *28*, 1705928; b) M. Tomczyk, I. Bretos, R. Jiménez, A. Mahajan, E. V. Ramana, M. L. Calzada, P. M. Vilarinho, *J. Mater. Chem. C* **2017**, *5*, 12529; c) C. S. Han, H. R. Choi, H. J. Choi, Y. S. Cho, *Chem. Mater.* **2017**, *29*, 5915; d) H. Yu, C.-C. Chung, N. Shewmon, S. Ho, J. H. Carpenter, R. Larrabee, T. Sun, J. L. Jones, H Ade, B. T. O'Connor, F. So, *Adv. Funct. Mater.* **2017**, *27*, 1700461; e) D. Pérez-Mezcua, I. Bretos, R. Jiménez, J. Ricote, R. J. Jiménez-Riobóo, C. G. da Silva, D. Chateigner, L. Fuentes-Cobas, R. Sirera, M. L. Calzada, *Sci. Rep.* **2016**, *6*, 39561; f) A. Llordés, Y. Wang, A. Fernandez-Martinez, P. Xiao, T. Lee, A. Poulain, O. Zandi, C. A. Saez-Cabezas, G. Henkelman, D. J. Milliron, *Nat. Mater.* **2016**, *15*, 1267; g) Y. Ji, Y. Yang, S.-K. Lee, G. Ruan, T.-W. Kim, H. Fei, S.-H. Lee, D.-Y. Kim, J. Yoon, J. M. Tour, *ACS Nano* **2016**, *10*, 7598; h) I. Bretos, R. Jiménez, D. Pérez-Mezcua, N. Salazar, J. Ricote, M. L. Calzada,

Adv. Mater. **2015**, *27*, 2608; i) T. Nakajima, T. Tsuchiya, *J. Mater. Chem. C* **2015**, *3*, 3809; j) I. Bretos, R. Jiménez, A. Wu, A. I. Kingon, P. M. Vilarinho, M. L. Calzada, *Adv. Mater.* **2014**, *26*, 1405.

[5] C. Linghu, S. Zhang, C. Wang, J. Song, *npj Flexible Electron.* **2018**, *26*, 6508.

[6] a) J. W. Park, B. H. Kang, H. J. Kim, *Adv. Funct. Mater.* **2019**, *30*, 1904632; b) I. Bretos, R. Jiménez, J. Ricote, M. L. Calzada, *Chem. Soc. Rev.* **2018**, *47*, 291; c) S. Diodati, P. Dolcet, M. Casarin, S. Gross, *Chem. Rev.* **2015**, *115*, 11449; d) H. Kozuka, *J. Mater. Res.* **2013**, *28*, 673; e) E. Fortunato, P. Barquinha, R. Martins, *Adv. Mater.* **2012**, *24*, 2945; f) K. K. Banger, Y. Yamashita, K. Mori, R. L. Peterson, T. Leedham, J. Rickard, H. Sirringhaus, *Nat. Mater.* **2011**, *10*, 45.

[7] I. Bretos, S. Diodati, R. Jiménez, F. Tajoli, J. Ricote, G. Bragaggia, M. Franca, M. L. Calzada, S. Gross, *Chem. - Eur. J.* **2020**, https://doi.org/10.1002/chem.202000448.

[8] T. G. Gutowski, M. S. Branham, J. B. Dahmus, A. J. Jones, A. Thiriez, *Environ. Sci. Technol.* **2009**, *43*, 1584.

[9] a) G. Catalan, J. F. Scott, *Adv. Mater.* **2009**, *21*, 2463; b) R. Ramesh, N. A. Spaldin, *Nat. Mater.* **2007**, *6*, 21.

[10] a) D. Pérez-Mezcua, R. Sirera, R. Jiménez, I. Bretos, C. De Dobbelaere, A. Hardy, M. K. Van Bael, M. L. Calzada, *J. Mater. Chem. C* **2014**, *2*, 8750; b) N. Martín-Arbella, I. Bretos, R. Jiménez, M. L. Calzada, R. Sirera, *J. Mater. Chem.* **2011**, *21*, 9051.

[11] a) I. Bretos, R. Jiménez, J. Ricote, M. L. Calzada, *Chem. - Eur. J.* **2020**, https://doi.org/10.1002/chem.202000244; b) E. Yarali, C. Koutsiaki, H. Faber, K. Tetzner, E. Yengel, P. Patsalas, N. Kalfagiannis, D. C. Koutsogeorgis, T. D. Anthopoulos, *Adv. Funct. Mater.* **2019**, *30*, 1906022; c) T. Nakajima, K. Shinoda, T. Tsuchiya, *Chem. Soc. Rev.* **2014**, *43*, 2027; d) Y.-H. Kim, J.-S. Heo, T.-H. Kim, S. Park, M.-H. Yoon, J. Kim, M. S. Oh, G.-R. Yi, Y.-Y. Noh, S. K. Park, *Nature* **2012**, *489*, 128.

[12] S. Park, K.-H. Kim, J.-W. Jo, S. Sung, K.-T. Kim, W.-J. Lee, J. Kim, H. J. Kim, G.-R. Yi, Y.-H. Kim, M.-H. Yoon, S. K. Park, *Adv. Funct. Mater.* **2015**, *25*, 2807.

[13] A. Varma, A. S. Mukasyan, A. S. Rogachev, K. V. Manukyan, *Chem. Rev.* **2016**, *116*, 14493.

[14] D. Sanchez-Rodriguez, J. Farjas, P. Roura, S. Ricart, N. Mestres, X. Obradors, T. Puig, *J. Phys. Chem. C* **2013**, *117*, 20133.

[15] M.-G. Kim, M. G. Kanatzidis, A. Facchetti, T. J. Marks, *Nat. Mater.* **2011**, *10*, 382.

[16] a) A. Sadlo, S. M. J. Beer, S. Rahman, M. Grafen, D. Rogalla, M. Winter, A. Ostendorf, A. Devi, *Eur. J. Inorg. Chem.* **2018**, *2018*, 1824; b) B. Malic, M. Kosec, I. Arcon, A. Kodre, *J. Eur. Ceram. Soc.* **2005**, *25*, 2241.

[17] N. Martín-Arbella, I. Bretos, R. Jiménez, M. L. Calzada, R. Sirera, */m. Ceram. Soc.* **2011**, *94*, 396.

[18] a) S. Mishra, E. Jeanneau, M. Rolland, S. Daniele, *RSC Adv.* **2016**, *6*, 1738; b) J. Le Bris, L. G. Hubert-Pfalzagraf, S. Daniele, J. Vaissermann, *Inorg. Chem. Commun.* **2007**, *10*, 80.

[19] a) K. E. Dettelbach, D. A. Salvatore, A. Bottomley, C. P. Berlinguette, *J. Mater. Chem. A* **2018**, *6*, 4544; b) I. W. Boyd, J. Y. Zhang, *Nucl. Instrum. Methods Phys. Res., Sect. B* **1997**, *121*, 349.

[20] E. Carlos, R. Branquinho, A. Kiazadeh, P. Barquinha, R. Martins, E. Fortunato, *ACS Appl. Mater. Interfaces* **2016**, *8*, 311000.

[21] P. Villars, K. Cenzual, *Pearson's Crystal Data: Crystal Structure Database for Inorganic Compounds (on DVD)*, ASM International, Materials Park, OH, USA **2018–19**.

[22] a) N. Deepak, P. Carolan, L. Keeney, P. F. Zhang, M. E. Pemble, R. Whatmore, *Chem. Mater.* **2015**, *27*, 6508; b) C. Gutiérrez-Lázaro, I. Bretos, R. Jiménez, J. Ricote, H. El Hosiny, D. Pérez-Mezcua, R. J. Jiménez-Riobóo, M. García-Hernández, M. L. Calzada, *J. Am. Ceram. Soc.* **2013**, *96*, 3061.

[23] I. Bretos, R. Jiménez, C. Gutiérrez-Lázaro, I. Montero, M. L. Calzada, *Appl. Phys. Lett.* **2014**, *104*, 092905.

[24] R. Jiménez, C. Alemany, M. L. Calzada, A. González, J. Ricote, J. Mendiola, *Appl. Phys. A* **2002**, *75*, 607.

[25] a) R. Nechache, C. Harnagea, S. Li, L. Cardenas, W. Huang, J. Chakrabartty, F. Rosei, *Nat. Photonics* **2015**, *9*, 61; b) S. Y. Yang, J. Seidel, S. J. Byrnes, P. Shafer, C.-H Yang, M. D. Rossell, P. Yu, Y.-H. Chu, J. F. Scott, J. W. AgerIII, L. W. Martin, R. Ramesh, *Nat. Nanotechnol.* **2010**, *5*, 143.

[26] a) W. X. Gao, R. Brennan, Y. Hu, M. Wuttig, G. L. Yuan, E. Quandt, S. Q. Ren, *Mater. Today* **2018**, *21*, 771; b) H. Huang, J. F. Scott, *Ferroelectric Materials for Energy Applications*, Wiley-VCH Verlag GmbH &Co. KGaA, Weinheim, Germany **2018**.

[27] L. Li, P. A. Salvador, G. S. Rohrer, *Nanoscale* **2014**, *6*, 24.

[28] a) S. J. A. Moniz, R. Quesada-Cabrera, C. S. Blackman, J. Tang, P. Southern, P. M. Weaver, C. J. Carmalt, *J. Mater. Chem. A* **2014**, *2*, 2922; b) F. Gao, X. Chen, K. Yin, S. Dong, Z. Ren, F. Yuan, T. Yu, Z. Zou, J.-M. Liu, *Adv. Mater.* **2007**, *19*, 2889.

[29] a) N. Vodisek, A. Suligoj, D. Korte, U. L. Stangar, *Materials* **2018**, *11*, 1945; b) W. Wang, T. Ai, Q. Yu, *Sci. Rep.* **2017**, *7*, 42615.